COMMUNICATION

Check for updates

Nanoparticle-assembled interconnected PbO$_{1.44}$ hollow spheres enabled by PVP-driven transformation of β-PbO$_2$ and self-sacrificial templating for superior lithium storage†

Xiaoxu Bo,*‡[a] Jiatong Zhang,‡[b] Qian Zhang,[b] Ruijie Wu,[b] Sheng Wang,[a] Shiqiang Zhao [ID] *[b] and Shun Wang [ID] *[b]

Lead oxides (PbO$_x$, $1 \leq x \leq 2$) are promising high-capacity and low-cost anodes for lithium ion batteries (LIBs). However, the huge lithiation-induced volume expansion of conventional large-sized PbO$_x$ particles leads to severe electrode pulverization with poor cycling stability. Herein, a rare mixed-valence PbO$_{1.44}$ with a unique hierarchical architecture of nanoparticle-assembled interconnected hollow spheres (denoted PbO$_{1.44}$ NAHSs) is crafted by

introducing polyvinylpyrrolidone (PVP) into the solution of generating β-PbO$_2$ microspheres (MSs), which is exploited for the first time as a potential advanced anode material for LIBs. Notably, an intriguing PVP-driven dissolution−recrystallization transformation process converting β-PbO$_2$ MSs into PbO$_{1.44}$ NAHSs is revealed by PVP-concentration and reaction-time control experiments, demonstrating the dual function of PVP as a mild reducing agent combined with it being a morphology regulator for the construction of PbO$_{1.44}$ NAHSs. Furthermore, a self-sacrificial templating mechanism is demonstrated for yielding the interconnected hollow structure of PbO$_{1.44}$ NAHSs. Remarkably, PbO$_{1.44}$ NAHSs deliver stable capacities of 561 and 453 mA h g^{-1} after 100 and 200 cycles at 50 and 500 mA g^{-1}, respectively, in sharp contrast to the performance of β-PbO$_2$ MSs (52 and 43 mA h g^{-1}). Structural and electrochemical measurements of the cycled electrodes indicate that the hollow and nanoarchitectural structure of PbO$_{1.44}$ NAHSs enables their superior cycling and rate capabilities, benefiting from the effectively buffered volume expansion and shortened lithium storage distance, respectively. As such, this work highlights a robust PVP-assisted strategy to fabricate rare mixed-valence PbO$_{1.44}$ NAHSs with outstanding electrochemical reactivity and mechanical robustness for lithium storage and various potential applications.

[a]*Department of Agriculture and Biotechnology, Wenzhou Vocational College of Science and Technology, Wenzhou 325006, P. R. China. E-mail: boxxsci@163.com*
[b]*Key Laboratory of Advanced Energy Storage and Conversion of Wenzhou, Key Laboratory of Carbon Materials of Zhejiang Province, College of Chemistry and Materials Engineering, Wenzhou University, Wenzhou 325035, P. R. China. E-mail: zhaosq@wzu.edu.cn, shunwang@wzu.edu.cn*
†Electronic supplementary information (ESI) available. See DOI: https://doi.org/10.1039/d4nr04763j
‡These authors contributed equally to this work.

Shiqiang Zhao is currently an Associate Professor and Dean of the Department of Energy Chemistry in the College of Chemistry and Materials Engineering at Wenzhou University. He earned his B.S. (2009) and Ph.D. (2017) degrees in Prof. Qiang Shen's group at Shandong University. He spent three semesters as a visiting Ph. D. student and then two years as a postdoctoral researcher in Prof. Zhiqun Lin's group in the School of Materials Science and Engineering at Georgia Institute of Technology (2015–2019). His research interests focus on the rational design, performance enhancement and electrochemical mechanisms of advanced electrode materials for alkali-ion batteries.

Shiqiang Zhao

1. Introduction

The ever-increasing demand for portable electronics with long service life and high power density has triggered the rapid development of high-performance energy storage technologies.[1,2] Among all of the commercial electrochemical power sources, lithium ion batteries (LIBs) have achieved great success due to their higher energy density, longer cycle life, and better environmental friendliness in contrast to most of the popular secondary batteries.[3,4] However, the low theoretical mass and volume capacities of commercial graphite anodes (*i.e.*, 372 mA h g^{-1} and 830 mA h cm^{-3}) seriously restrict the property improvement of next-generation LIBs.[5,6]

In recent decades, elements in Group IVA (*i.e.*, Si, Ge, Sn and Pb) and their compounds have attracted wide attention as promising high-capacity anodes for LIBs based on their alloying–dealloying reaction mechanisms with the advantages of suitable low-voltage plateaus ($\sim$0.5 V *vs.* Li$^+$/Li), low cost and abundance.[7,8] Therein, lead oxides (PbO$_x$, $1 \leq x \leq 2$) possess higher theoretical mass and especially volumetric specific capacities (*e.g.*, PbO (769 mA h g^{-1} and 7329 mA h cm^{-3}) and PbO$_2$ (941 mA h g^{-1} and 8827 mA h cm^{-3})) than graphite, based on the conversion-combined alloying–dealloying reactions of PbO$_x$ + 2xLi$^+$ + 2$xe^- \rightleftharpoons$ Pb + xLi$_2$O ($1 \leq x \leq 2$) and Pb + yLi$^+$ + $ye^- \rightleftharpoons$ Li$_y$Pb ($0 \leq y \leq 4.4$), respectively.[9–12] Nevertheless, due to the sluggish electrochemical reaction kinetics and huge volume expansion, the conventionally fabricated PbO$_x$ particles with large-sized bulk structures usually exhibit poor cycling stability and rate capability.[13–15] Therefore, rational approaches to the design of structures and compositions of PbO$_x$-based materials are crucial to enhance their lithium storage performances for realizing their practical application as anodes of LIBs.[16–19]

As a post-transition metal with the electronic configuration of 6s^{2}6p^2, Pb has many types of oxides including PbO, PbO$_2$ and various mixed-valence compounds (*i.e.*, Pb$_2$O$_3$, Pb$_3$O$_4$ and non-stoichiometric PbO$_x$ ($1 < x < 2$)). Due to their outstanding properties in optical, ferroelectric, dielectric, energy-storage and oxygen-sensing fields, PbO$_x$-based materials have been widely used in the industrial fields of lead acid batteries, paints, glasses and so on.[20–22] As a result, the fabrication strategies and crystallization behaviors of PbO$_x$ have always been hot research topics.[23,24] For electrochemical syntheses, orthorhombic α-PbO$_2$ and tetragonal β-PbO$_2$ can be generally obtained in a strong acidic medium and an alkaline or neutral medium, respectively.[25] In contrast to electrochemical methods, solution-based chemical routes for synthesizing PbO$_x$ are more controllable in terms of the structure–composition design and easier to scale up.[26–28] However, up to now, the preparation of phase-pure non-stoichiometric PbO$_x$ ($1 < x < 2$) by the more popular solution-based methods has rarely been reported, limiting their structural analysis, property investigation and application exploration.[20–28]

As for the mixed-valence oxides of PbO$_x$ (*e.g.*, Pb$_2$O$_3$, Pb$_3$O$_4$ and non-stoichiometric PbO$_x$ ($1 < x < 2$)), the non-integral x value can be regarded as an incomplete oxidation of Pb^{2+} or a partial reduction of Pb^{4+} in the crystallization process of PbO$_x$ ($1 < x < 2$), occasionally found in the heat-treatment process of solid-state precursors of PbO$_2$ or PbO. For example, PbO$_{1.55}$ has been captured during the heat-treatment of chemically produced β-PbO$_2$ at 400 °C, which is recognized as one of the crystalline intermediates of partially reduced β-PbO$_2$.[29] Similarly, serial crystalline phases of PbO$_x$ ($1 < x < 2$) have also been detected during the air-oxidizing of tetragonal PbO, resulting in PbO$_{1.548}$ and PbO$_{1.333}$ at 286 and 351 °C, respectively.[30] Therein, the created PbO$_x$ series ($1.41 < x < 1.57$) exhibited similar X-ray diffraction (XRD) patterns to that of cubic PbO$_{1.44}$ ($a = 4.9525$ Å, JCPDS no. 27-1201) obtained after annealing PbO at 293 °C for 180 h in an air atmosphere. A thin film of well-defined PbO$_{1.44}$ was prepared by reactive direct current magnetron sputtering from a metallic lead target onto Si (100) wafers and glass substrates in a precisely controlled flow of an oxygen–argon mixture.[31] Nevertheless, there has been no report concerning the fabrication of PbO$_{1.44}$ with high purity, high crystallinity and fine structure *via* a facile solution-based method until now. The solution-based method is widely used for the synthesis of ultra-fine powders in research and industry due to its significant advantages of high controllability, low cost and high reaction efficiency.[3,5,7,8] First, the solution-based method can control the reaction rate, particle size distribution and morphology by adjusting the reaction conditions and additives, thus achieving precise control of the products. Second, compared with other synthesis methods (*e.g.* gas-phase method and solid-phase method), the equipment cost for solution reaction is relatively low with simple operation, so it is easier to achieve large-scale industrial production. Third, the reaction speed of solution-based synthesis is generally fast with high reaction efficiency to quickly obtain the desired products.

In this work, a facile polyvinyl pyrrolidone (PVP)-assisted hydrothermal route has been rationally developed to produce pure-phase cubic PbO$_{1.44}$ particles ($\sim$1 μm in diameter) with high crystallinity and a unique structure of nanoparticles ($\sim$50 nm in diameter) assembled into interconnected hollow spheres (denoted PbO$_{1.44}$ NAHSs), which have been studied for the first time as promising anode materials for LIBs. As a polymeric surfactant, PVP generally acts as a soft-templating and capping agent for the crystallization and self-assembly of inorganic particles.[32–34] Besides, PVP has also been successfully used for the controllable synthesis of noble metal particles (*e.g.*, Ag, Au, Pd and Pt) by serving as a mild reductant for the slow reduction of water-soluble metal salts.[35–37] As expected, by introducing PVP as a mild reductant into the hydrothermal reaction solution for the preparation of β-PbO$_2$ microspheres (denoted β-PbO$_2$ MSs), an intriguing PVP-driven dissolution–recrystallization transformation process converting β-PbO$_2$ MSs into PbO$_{1.44}$ NAHSs has been discovered and well proven by a PVP-concentration control experiment. More importantly, time-dependent experiments demonstrate a self-sacrificial templating mechanism for the formation of the unique interconnected structure of PbO$_{1.44}$ NAHSs. Therefore, PVP serves as both a mild reductant and a morphology regulator for the formation of nanostructured PbO$_{1.44}$ NAHSs.

Notably, PbO$_{1.44}$ NAHSs exhibit outstanding cycling and rate capabilities with stable capacities of 561 and 453 mA h g^{-1} after 100 and 200 cycles at 50 and 500 mA g^{-1}, respectively, in sharp contrast to the performance of β-PbO$_2$ MSs (52 and 43 mA h g^{-1}). As uncovered by systematic structural and electrochemical investigations, the superior electrochemical properties of PbO$_{1.44}$ NAHSs can be attributed to the unique interconnected hollow structure assembled from nanoparticles. First, the secondary nanoparticles shorten the lithium storage distance and enlarge the contact area with the electrolyte for sufficient lithium storage reaction and fast electrochemical kinetics, giving rise to the high capacity and

excellent rate capability, respectively. Second, the interconnected hollow structure effectively buffers the lithiation–delithiation-induced volume expansion–shrinkage of $PbO_{1.44}$ NAHSs, enabling the ultra-high structrual robustness of the electrode and thus the outstanding cycling performance. As such, this study underscores a robust PVP-assisted hydrothermal route to prepare high-quality $PbO_{1.44}$ NAHSs with excellent electrochemical reactivity and mechanical robustness for a wide range of diverse potential applications including lithium-ion batteries, lead-acid batteries, catalysis, sensing, and so on.

2.   Results and discussion

2.1.   PVP-driven transformation of β-PbO$_2$ MSs into PbO$_{1.44}$ NAHSs

Scanning electron microscopy (SEM, Fig. 1a–d and S1†) and transmission electron microscopy (TEM, Fig. 1e–h) images reveal that the 7 h hydrothermal reaction of lead acetate, sodium hydroxide and ammonium persulfate in the presence of polyvinylpyrrolidone K30 (PVP, 3 g L^{-1}) at 120 °C gave rise to a product with a unique structure of nanoparticle-assembled hollow spheres (NAHSs). Notably, all the hollow
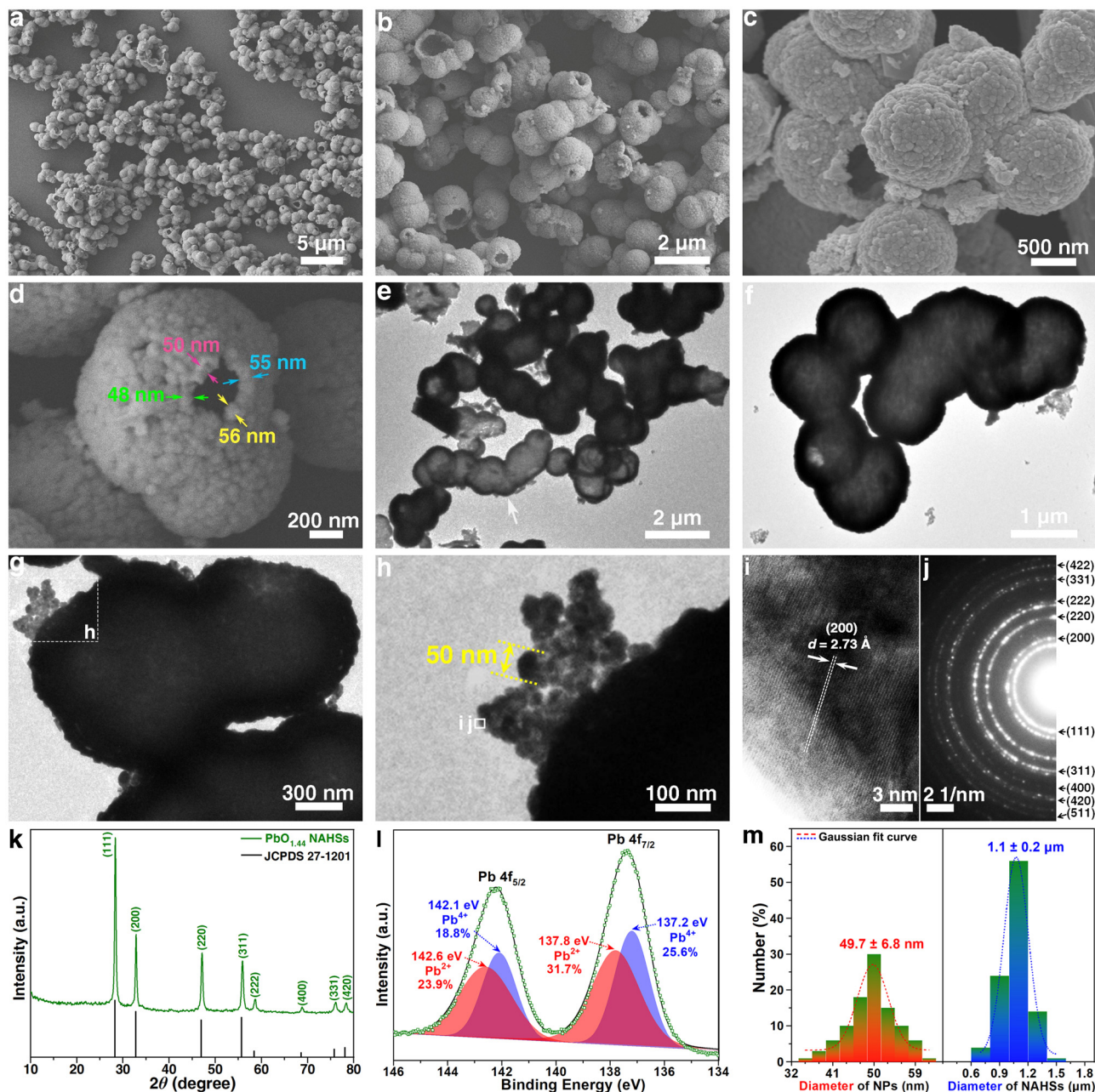
Fig. 1 Structural characterization of $PbO_{1.44}$ NAHSs. (a–d) SEM and (e–i) TEM images. (j) SAED pattern, (k) XRD pattern and (l) XPS spectrum of $PbO_{1.44}$ NAHSs. (m) Diameter distributions of secondary $PbO_{1.44}$ nanoparticles (left panel) and $PbO_{1.44}$ NAHSs (right panel).

spheres are interconnected with adjacent ones, as distinctly demonstrated by the TEM images of Fig. 1e–g. The high magnification SEM images (Fig. 1d and S1c–f†) clearly show that the hollow spheres are assembled from ultra-fine nanoparticles. The high-resolution TEM (HRTEM) image (Fig. 1i), selected area electron diffraction (SAED) pattern (Fig. 1j) and powder X-ray diffraction (XRD) pattern (Fig. 1k) of the product indicate the pure-phase, high-crystallinity and polycrystalline character of cubic $PbO_{1.44}$ crystals (a = 5.469 Å, JCPDS no. 27-1201). In the X-ray photoelectron spectroscopy (XPS) spectrum of Pb 4f of the $PbO_{1.44}$ NAHSs (Fig. 1l), the Pb $4f_{5/2}$ and Pb $4f_{7/2}$ peaks can be divided into two pairs of peaks at 142.6 and 137.8 eV corresponding to Pb^{2+} and at 142.1 and 137.2 eV corresponding to Pb^{4+}, respectively. According to the relative area percentages of the Pb 4f peaks of $PbO_{1.44}$ NAHSs (i.e., Pb^{2+} (55.6%) and Pb^{4+} (44.4%)), a chemical formula of $PbO_{1.444}$ can be estimated, which is almost identical to the stoichiometric ratio of $PbO_{1.44}$. From the particle size statistics based on the SEM and TEM images (Fig. 1a–h and S1†), the average diameters of $PbO_{1.44}$ NAHSs and secondary nanoparticles that are assembled into $PbO_{1.44}$ NAHSs are 1.1 ± 0.2 μm and 49.7 ± 6.8 nm (Fig. 1m), respectively.

As a well-known dispersant or colloidal stabilizer of nanoparticles, the polymeric surfactant PVP has been popularly involved in the size and morphology controllable syntheses of a variety of functional micro/nano particles.[38–42] Besides, it has been proved that the abundant carbonyl groups of PVP can be oxidized to carboxyl or ester groups, endowing PVP with mild reducibility.[35] In order to clarify the crucial roles of PVP in the formation of $PbO_{1.44}$ NAHSs, a series of control experiments that involve regulating PVP concentrations (i.e., 0, 0.5, 1.0, 1.5, 2.0 and 2.5 g L^{-1}) were performed (Fig. 2 and S2–S8†). As a blank experiment in the absence of PVP, the reaction of lead acetate, sodium hydroxide and ammonium persulfate resulted in the generation of inhomogeneous large-sized solid β-PbO_2 microspheres (denoted β-PbO_2 MSs) (Fig. 2a, b, l and S2†) with an average diameter of 3.9 ± 1.5 μm (Fig. S2f†). The Pb 4f XPS spectrum of β-PbO_2 MSs (Fig. S3†) shows Pb $4f_{5/2}$ and Pb $4f_{7/2}$ peaks at 142.1 and 137.2 eV, corresponding to Pb^{4+} in β-PbO_2.

Interestingly, after introducing a small amount of PVP (0.5 g L^{-1}) into the reaction solution for producing β-PbO_2, a mixture of β-PbO_2 MSs (primary) and $PbO_{1.44}$ NAHSs (secondary) was created (Fig. 2c, l and S4†). Moreover, along with the gradually increased concentrations of PVP to 1.0, 1.5, 2.0, and 2.5 g L^{-1}, the amount ratios of $PbO_{1.44}$ NAHSs in the mixed products keep on increasing (Fig. 2d–k and S5–S8†), in accordance with the continuously strengthening XRD peaks of $PbO_{1.44}$ and weakening XRD peaks of β-PbO_2 (Fig. 2l). It is noteworthy that some $PbO_{1.44}$ NAHSs grow in situ on the β-PbO_2 MSs, as indicated by the white arrows in Fig. 2d and e, implying the close relationship between $PbO_{1.44}$ NAHSs and β-PbO_2 MSs. In addition, the fragmentary particles of β-PbO_2 MSs can be observed in the mixtures as indicated by the white arrows in Fig. 2g, i and k, suggesting a PVP-driven reduction combined dissolution process of β-PbO_2 causing the transformation of β-PbO_2 MSs into $PbO_{1.44}$ NAHSs. Therefore, it can be concluded that PVP serves as a dual-functional additive acting as a mild reducing agent combined with being a morphology regulator to induce the conversion of β-PbO_2 MSs into $PbO_{1.44}$ NAHSs.

2.2. Self-sacrificial templating formation of the interconnected hollow structure of $PbO_{1.44}$ NAHSs

To elucidate the formation mechanism of the unique architecture of nanoparticle-assembled interconnected hollow spheres of $PbO_{1.44}$ NAHSs, time-dependent experiments were performed over designated incubation times of 1, 3 and 5 h (Fig. 3 and S9–S11†). After reaction for 1 h, amorphous mixed particles were obtained (Fig. 3a–c, l and S9†), including a large amount of randomly aggregated solid spheres assembled from nanoparticles (Fig. 3c and S9b†) and a small amount of large irregular particles (as indicated by the white arrows in Fig. 3a and b). Then, after 3 h of reaction (Fig. 3d–h, l and S10†), the hydrothermal solution-mediated dissolution–recrystallization took place from the inside to the outside of the amorphous solid spheres formed after 1 h, generating interconnected $PbO_{1.44}$ hollow spheres with thick shells (Fig. 3f and g). Notably, the SAED pattern of a solid microsphere from the 3 h product confirms that the microspheres in the intermediate mixtures are β-PbO_2. Due to the gradual PVP-driven reduction and dissolution of β-PbO_2 MSs and hydrothermal-induced dissolution–recrystallization from the inside out of $PbO_{1.44}$ NAHSs, a mixture of highly crystalline $PbO_{1.44}$ NAHSs (primary) with thinner shells and a small amount of small irregular crumbs of β-PbO_2 MSs (secondary, as indicated by the white arrows in Fig. 3i and j) were obtained after 5 h (Fig. 3i–l and S11†). Finally, pure phase $PbO_{1.44}$ NAHSs were produced after 7 h of the hydrothermal reaction (Fig. 1 and S1†).

SEM images of the representative intermediate particles obtained after 1, 3 and 5 h visually demonstrate the structural evolution of $PbO_{1.44}$ NAHSs (Fig. 4a–c) and β-PbO_2 MSs (Fig. 4d–f). A typical hydrothermal-driven Ostwald ripening combined with a self-sacrificial templating mechanism accounts for the formation of $PbO_{1.44}$ NAHSs.[43] Aggregated amorphous solid spheres assembled from nanoparticles (denoted amorphous $PbO_{1.44}$ NASs) were formed after 1 h (Fig. 4a). Then, the hydrothermal environment induced the dissolution of the inner smaller nanoparticles, which were initially deposited from the solution, and then the recrystallization on the surfaces of later deposited larger nanoparticles, giving rise to the formation of $PbO_{1.44}$ NAHSs with thick shells (~250–320 nm) after 3 h of reaction (Fig. 4b).[43,44] As the Ostwald ripening process continued, the shell thicknesses of the $PbO_{1.44}$ NAHSs continued to decrease to ~110–140 nm for the 5 h intermediate (Fig. 4c) and then ~50 nm for the 7 h product (Fig. 1d). Therein, due to the dissolution of the nanoparticles at the contact areas of randomly aggregated spheres formed after 1 h, the unique interconnected hollow structure is created.[44] As for the β-PbO_2 MSs, a PVP-driven progressive dissolution process was observed along with extended reaction
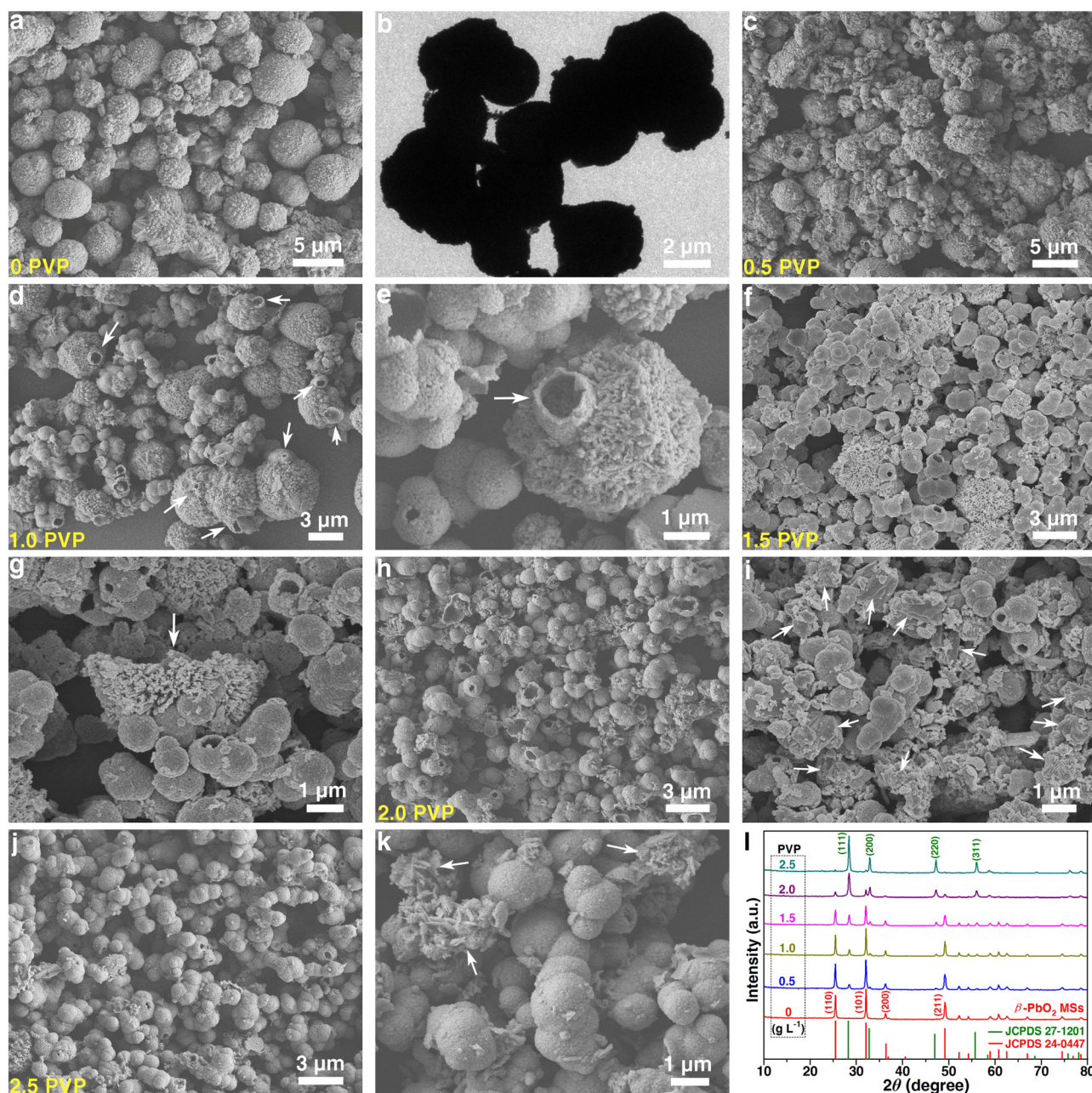
Fig. 2 Effect of PVP concentrations on the formation of PbO$_{1.44}$ NAHSs. (a) SEM and (b) TEM images of β-PbO$_2$ MSs. (c–k) SEM images and (l) XRD patterns of the mixtures of β-PbO$_2$ MSs and PbO$_{1.44}$ NAHSs obtained in the presence of (c) 0.5, (d and e) 1.0, (f and g) 1.5, (h and i) 2.0 and (j and k) 2.5 g L^{-1} PVP.

times, that is, from complete MSs (1 h, Fig. 4d) to incomplete MSs (3 h, Fig. 4e) and then to irregular fragments (5 h, Fig. 4f), which finally disappeared at 7 h (Fig. 1a, k and 3l). The structure formation mechanism of PbO$_{1.44}$ NAHSs is concisely illustrated in Fig. 4g. The weak reducing agent of PVP induces the progressive reduction and dissolution of β-PbO$_2$ MSs and simultaneous recrystallization on the PbO$_{1.44}$ NAHSs. Furthermore, the Ostwald ripening process from the inside outwards of the aggregated spheres generated after 1 h triggers

a self-sacrificial templating mechanism that constructs the interconnected hollow structure of PbO$_{1.44}$ NAHSs.[43,44]

2.3. Superior lithium storage capability of PbO$_{1.44}$ NAHSs

The electrochemical properties of PbO$_{1.44}$ NAHSs and β-PbO$_2$ MSs were examined using lithium cell models within a potential window of 0.01–3.0 V vs. Li$^+$/Li.[45,46] As an anode material of LIBs, PbO$_{1.44}$ NAHSs exhibited outstanding cycling stability at 50 (Fig. 5a) and 500 mA g^{-1} (Fig. 5b) with ultra-stable
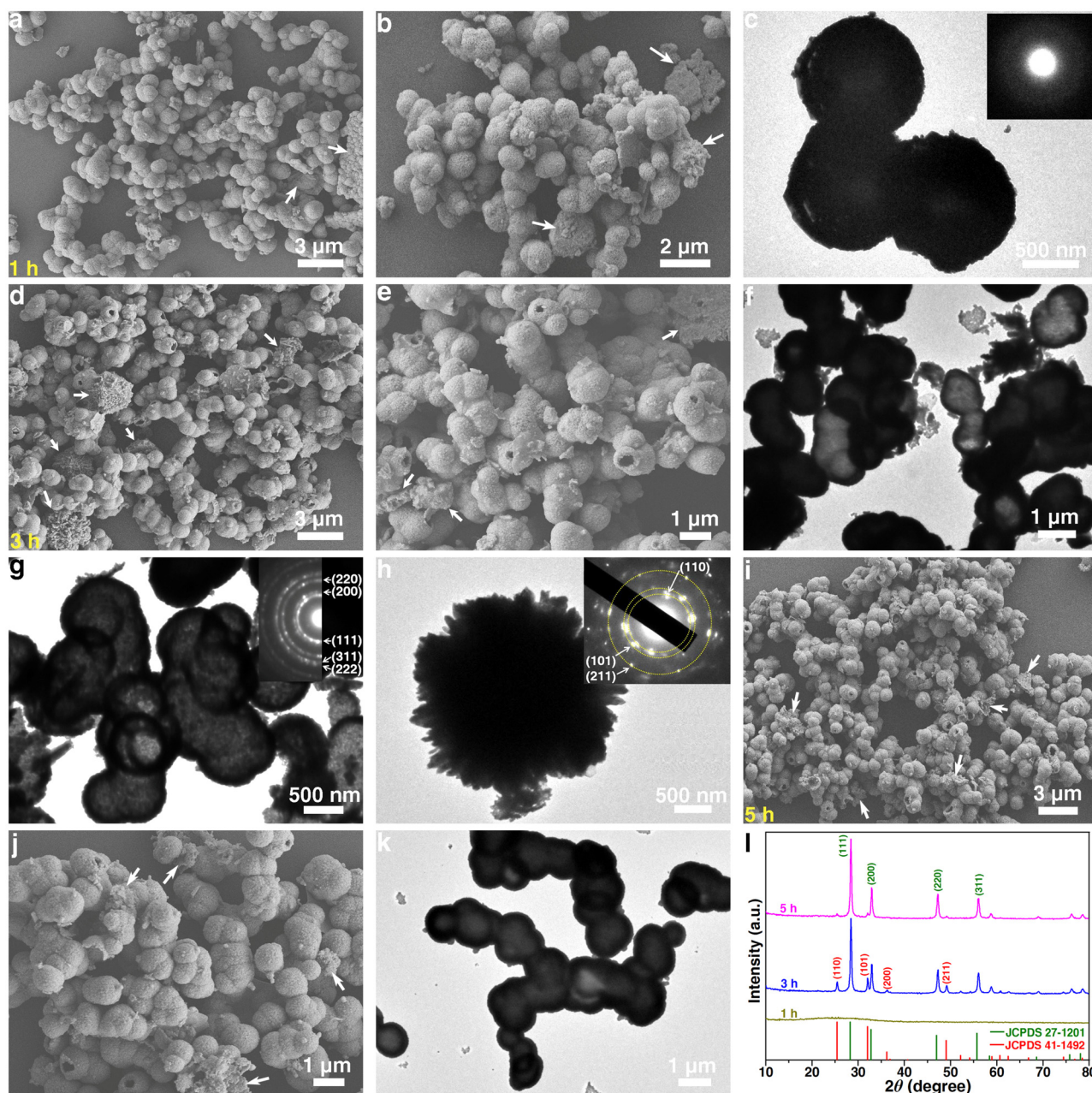
Fig. 3 Effect of reaction time on the formation of $PbO_{1.44}$ NAHSs. (a, b, d, e, i, j) SEM and (c, f, g, h, k) TEM images and (l) XRD patterns of the intermediate mixtures of $PbO_{1.44}$ NAHSs and β-PbO_2 MSs obtained after different reaction times of (a–c) 1, (d–h) 3 and (i–k) 5 h. Insets in (c, g, and h) are the corresponding SAED patterns of the samples.

capacities of 561 and 453 mA h g^{-1} after 100 and 200 cycles, respectively, in sharp contrast to the β-PbO_2 MSs (52 and 43 mA h g^{-1}). It is noteworthy that the capacities of $PbO_{1.44}$ NAHSs at the high current rate (C-rate) of 500 mA g^{-1} show a continuously increasing trend, from 412 mA h g^{-1} at the second discharge to 453 mA h g^{-1} at the 200th discharge. This can reasonably be attributed to the electrochemical activation of the electrode along with increased cycle numbers, due to the gradual perfection of the SEI layer and the progressive full penetration of the electrolyte with improved ionic conductivity

for enhanced reaction kinetics.[5–8] As expected, $PbO_{1.44}$ NAHSs also exhibited markedly enhanced rate capability at various C-rates compared with that of β-PbO_2 MSs (Fig. 5c). At a C-rate of 50 mA g^{-1}, $PbO_{1.44}$ NAHSs yielded an initial Coulomb efficiency (ICE) of 69.5%, with initial discharge/charge capacities of 893/621 mA h g^{-1}, respectively, which is much higher than the ICE of β-PbO_2 (54.4%). Even at a high C-rate of 1000 mA g^{-1}, $PbO_{1.44}$ NAHSs delivered a satisfactory capacity of 351 mA h g^{-1} on the 50th cycle, 4.4 times higher than that of β-PbO_2 MSs (79 mA h g^{-1}). When the C-rate was returned to
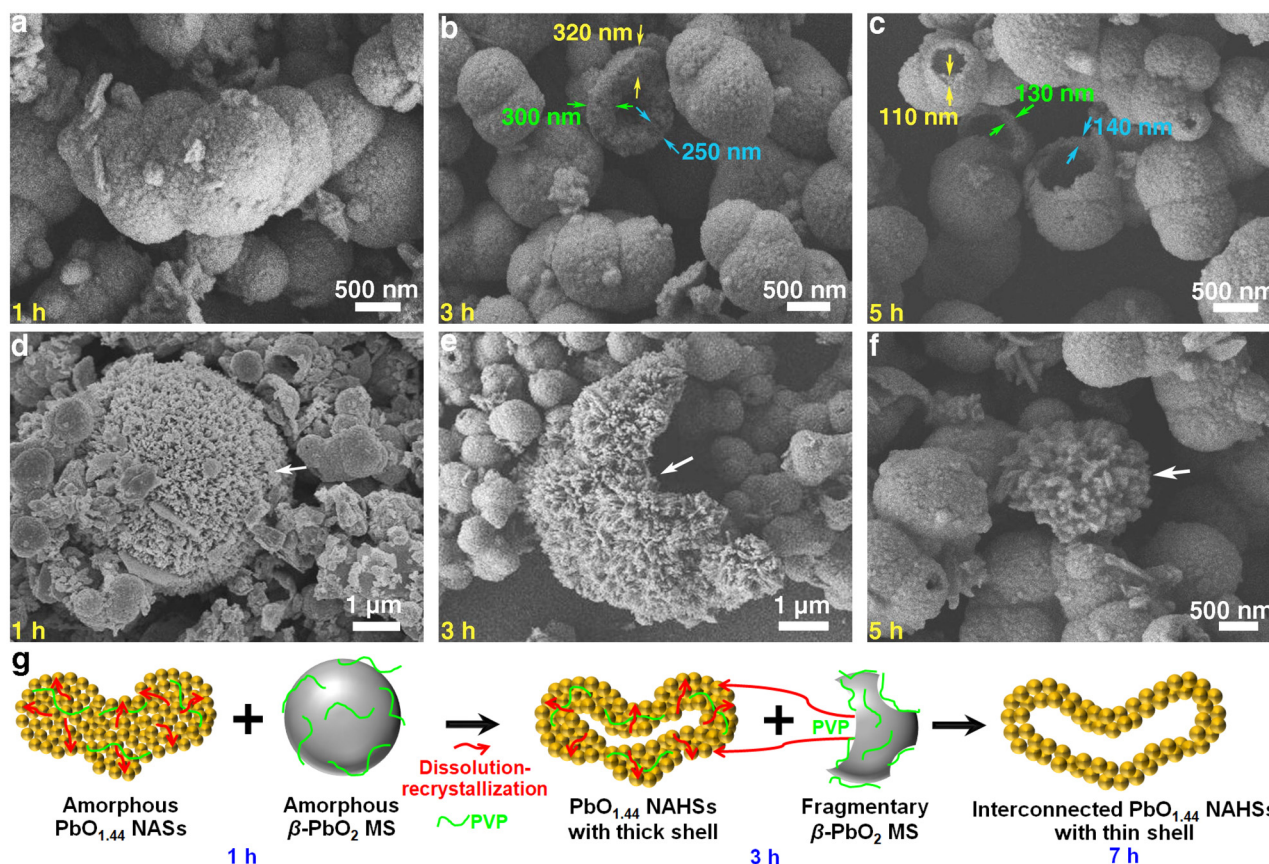
Fig. 4 Formation mechanism of PbO$_{1.44}$ NAHSs. SEM images of representative intermediate particles of (a–c) PbO$_{1.44}$ NAHSs and (d–f) β-PbO$_2$ MSs obtained after different reaction times of (a and d) 1, (b and e) 3 and (c and f) 5 h. (g) Schematic illustration of the formation mechanism of PbO$_{1.44}$ NAHSs.

50 mA g^{-1} after 60 cycles, the capacity of PbO$_{1.44}$ NAHSs successfully recovered to a high value of 623 mA h g^{-1} on the 90th cycle, which is almost the same as the first charge capacity (*i.e.*, 621 mA h g^{-1}), demonstrating the excellent capacity retention ability of PbO$_{1.44}$ NAHSs even after cycling at various C-rates.

To understand the electrochemical behaviors of PbO$_{1.44}$ NAHSs and β-PbO$_2$ MSs, the charge–discharge profiles (Fig. 5d and e) and cyclic voltammetry (CV) curves (Fig. 5f and g) were comparatively investigated. During the first cycles, the discharge capacities being higher than the charge capacities for both PbO$_{1.44}$ NAHSs and β-PbO$_2$ MSs can be primarily attributed to the irreversible formation of solid electrolyte interphase (SEI) layers on the electrodes, in agreement with the significant degradation of the discharge plateaus at 1.3 and 0.1 V (Fig. 5d) and the corresponding anodic peaks at 1.22 and 0.11 V (Fig. 5f) of PbO$_{1.44}$ NAHSs in the first lithiation process.[47] Similar decay trends in the related discharge plateaus and anodic peaks also occurred in the case of β-PbO$_2$ MSs (Fig. 5e and g). Remarkably, after the first discharge process, the charge–discharge profiles (Fig. 5d) and CV curves (Fig. 5f) of PbO$_{1.44}$ NAHSs are almost overlapped with each other, indicating the excellent reversibility of the lithiation–delithiation reac-

tions on the PbO$_{1.44}$ NAHSs electrode. According to the reports about PbO$_x$-based anodes for LIBs, the three pairs of discharge/charge plateaus (0.5/0.6, 0.4/0.5 and 0.3/0.4 V) and anodic/cathodic peaks below 0.7 V (*i.e.*, 0.53/0.63, 0.35/0.51 and 0.28/0.42 V) for PbO$_{1.44}$ NAHSs can be assigned to the reversible alloying/dealloying reactions in Pb.[9,10] In addition, the discharge plateau (1.5 V)/anodic peak (1.52 V) and charge plateaus (1.2 and 1.6 V)/cathodic peaks (1.26 and 1.61 V) in the 0.7–1.7 V range (Fig. 5d and f) can be attributed to the conversion reactions between Pb and PbO$_{1.44}$.[11,12]

In stark contrast to the outstanding electrochemical reversibility of PbO$_{1.44}$ NAHSs, the lengths of the discharge/charge plateaus (Fig. 5e) and the intensities of the anodic/cathodic peaks (Fig. 5g) of β-PbO$_2$ MSs continue to decay with increasing cycle numbers. Finally, there is almost no voltage plateau on the 50th cycle at 50 mA g^{-1} for β-PbO$_2$ MSs (Fig. 5e). More importantly, the decay rate of the discharge/charge plateaus of β-PbO$_2$ MSs (Fig. 5i) is much faster than that of PbO$_{1.44}$ NAHSs (Fig. 5h) along with increased C-rates, as obviously exhibited in the contrasting differential capacity *versus* voltage (dQ/dV) curves of the discharge profiles of PbO$_{1.44}$ NAHSs (Fig. 5j) and β-PbO$_2$ MSs (Fig. 5k). Notably, for both β-PbO$_2$ MSs and PbO$_{1.44}$ NAHSs, a faster degradation rate can be observed for
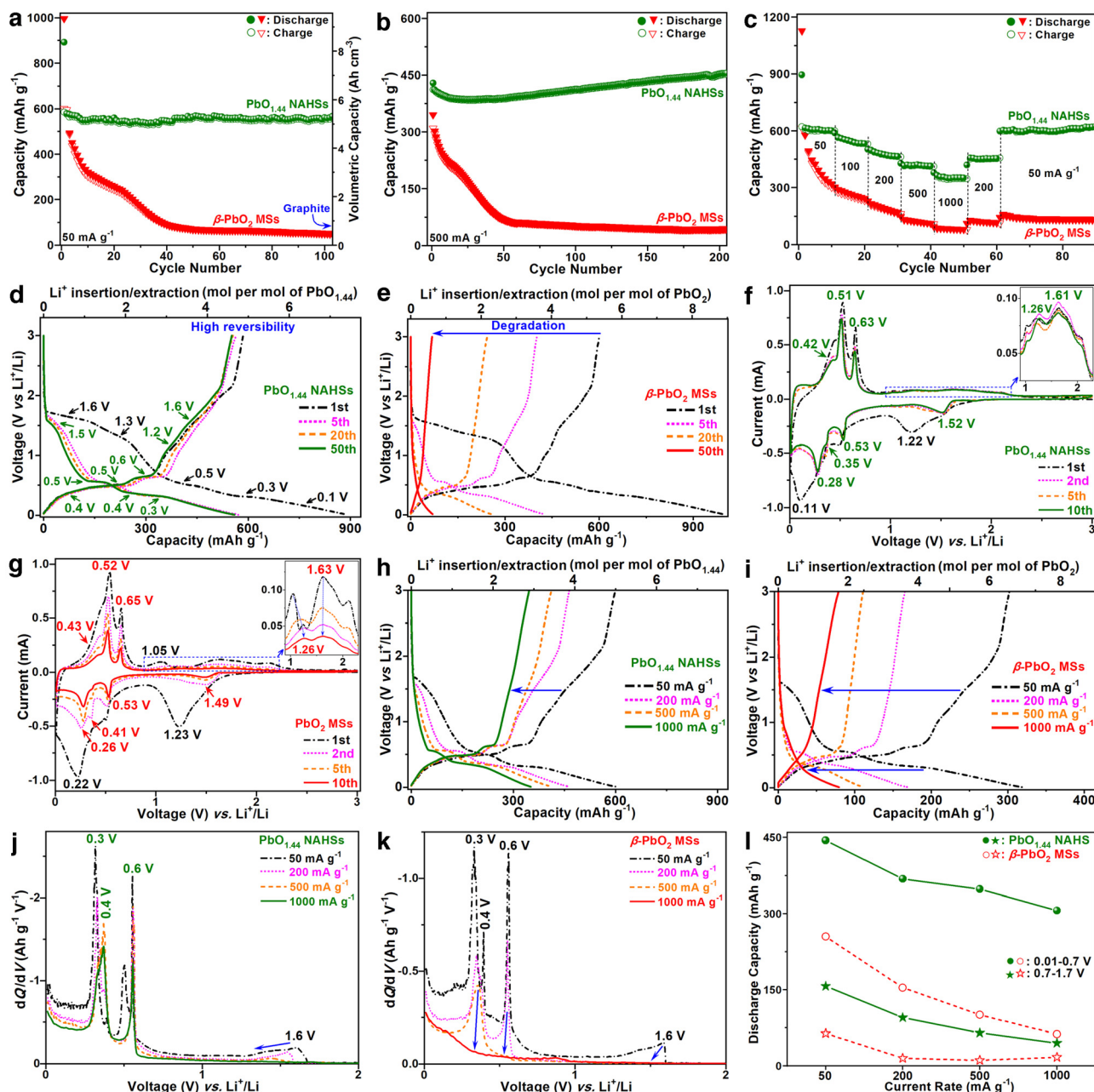
Fig. 5 Superior electrochemical performance of $PbO_{1.44}$ NAHSs compared to that of β-PbO_2 MSs. (a and b) Cycling and (c) rate performances of $PbO_{1.44}$ NAHSs and β-PbO_2 MSs as anodes of LIBs at designated C-rates. (d and e) Discharge–charge profiles at 50 mA g^{-1} and (f and g) CV curves at 0.2 mV s^{-1} of (d and f) $PbO_{1.44}$ NAHSs and (e and g) β-PbO_2 MSs. (h and i) Discharge–charge profiles, (j and k) dQ/dV curves of the discharge profiles and (l) comparison of the discharge capacities in the different voltage ranges of 0.01–0.6 and 0.6–1.7 V at different C-rates of (h and j) $PbO_{1.44}$ NAHSs and (i and k) β-PbO_2 MSs.

the plateaus in the voltage range of 0.7–1.7 V than that in the 0.01–0.7 V range along with increased C-rates, corresponding to the conversion reaction of PbO_x and the alloying–dealloying reaction of Pb, respectively. This suggests that the kinetics of the conversion reaction is slower than that of the alloying–dealloying reaction.[7,9] The capacities at different C-rates of the discharge profiles in the two voltage ranges of 0.01–0.7 V and 0.7–1.7 V are statistically analyzed as shown in Fig. 5l. The

long Li$^+$/e$^-$ transport distance of large-sized bulk-structured β-PbO_2 MSs leads to the poor kinetics in both conversion and alloying–dealloying reactions with rapidly decaying capacities along with increasing C-rates (Fig. 5l). Remarkably, $PbO_{1.44}$ NAHSs demonstrate an apparently improved stability in the discharge capacities from the plateaus over the voltage range of 0.01–0.7 V, corresponding to the alloying reaction of Pb, which contributes the major capacity at low and especially

high C-rates. Namely, the superior lithium storage capability of PbO$_{1.44}$ NAHSs can be primarily attributed to the much higher alloying–dealloying reaction kinetics than that of β-PbO$_2$ MSs, benefiting from the nanoparticle-assembled hollow structure with rich channels and short distances for the fast Li$^+$ transfer.

To clarify the performance enhancement mechanisms of PbO$_{1.44}$ NAHSs, systematic characterization studies of the cycled electrodes were performed, such as galvanostatic intermittent titration (GITT) measurements (Fig. 6a–d), electrochemical impedance spectroscopy (EIS) measurements (Fig. 6e), capturing SEM (Fig. 6f, k, S12 and S13†) and TEM (Fig. 6g and h) images, an SAED pattern (Fig. 6i) and the XPS spectrum (Fig. 6j). Fig. 6a and c show the potential response curves of PbO$_{1.44}$ NAHSs and β-PbO$_2$ MSs from the GITT measurements taken during the 10th discharge–charge processes at 50 mA g^{-1} as anodes of LIBs, respectively. Notably, the overpotentials of PbO$_{1.44}$ NAHSs remain at a lower level than those of β-PbO$_2$ MSs at the same discharge/charge state, especially in the high voltage ranges for the conversion reaction, suggesting a higher Li$^+$ ion conductivity and a lower polarization of PbO$_{1.44}$ NAHSs than those of β-PbO$_2$ MSs. Assuming that the Li$^+$ transfer satisfies Fick's second law, the Li$^+$ diffusion coefficient (D_{Li^+}) can be calculated by the equation of $D = \frac{4}{\pi\tau}\left(\frac{m_B V_m}{M_B S}\right)^2\left[\frac{\Delta E_s}{\Delta E_\tau}\right]^2$, $\left(\tau \ll \frac{L^2}{D}\right)$, where τ, L and S represent the constant current titration time, diffusion length and electrode surface area, ΔE_s and ΔE_τ refer to the steady-state voltage change after a current disturbance and voltage change during the constant current titration, and m_B, V_m and M_B are the molar mass, volume and molecular mass of PbO$_{1.44}$ or β-PbO$_2$, respectively.[48] The average D_{Li^+} values of 1.2 × 10^{-11} cm^2 s^{-1} and 1.7 × 10^{-11} cm^2 s^{-1} of PbO$_{1.44}$ NAHSs for the alloying and dealloying reaction processes (Fig. 6b and d) are approximately one order of magnitude higher than those of β-PbO$_2$ MSs (1.6 × 10^{-12} and 1.9 × 10^{-12} cm^2 s^{-1}), respectively. This firmly demonstrates the excellent alloying–dealloying reaction kinetics of PbO$_{1.44}$ NAHSs, which accounts for the high capacity and outstanding rate capability. The Nyquist plots of the freshly assembled cells of PbO$_{1.44}$ NAHSs and β-PbO$_2$ MSs are fitted according to the equivalent circuit (inset in Fig. 6e), where R_s, R_{ct}, Z_w and CPE represent the electrolyte resistance, charge transfer resistance, Warburg impedance and constant phase element, respectively.[49] The estimated R_{ct} of PbO$_{1.44}$ NAHSs (118 Ω) is about a quarter of that of β-PbO$_2$ MSs (426 Ω), demonstrating the strengthened charge transfer conductivity of PbO$_{1.44}$ NAHSs with their special hierarchical hollow nanoarchitecture.[43,44]

To verify the electrode stability enhancement mechanism, the contrasting structures of cycled electrodes of PbO$_{1.44}$ NAHSs and β-PbO$_2$ MSs (Fig. 6f–k, S12 and S13†) were investigated after the rate performance tests (Fig. 5c). Encouragingly, the cycled electrode of PbO$_{1.44}$ NAHSs is flat and compact (Fig. 6f, S12, S14a and S15a†). The interconnected hollow interior of PbO$_{1.44}$ NAHSs can robustly buffer the volume expansion and shrinkage induced by the repeated lithiation and delithiation processes, respectively, to stabilize the structure of PbO$_{1.44}$ NAHSs (Fig. 6f and g) and enhance the robustness of the whole electrode. The HRTEM image (Fig. 6h) and SAED pattern (Fig. 6i) of the cycled PbO$_{1.44}$ NAHSs show the reversible generation of the PbO$_{1.44}$ phase after the 90th charging process, with distinguished lattice fringes of the PbO$_{1.44}$-based (111) facet (d = 3.16 Å) and diffraction rings of the (111), (200), (220), (222) and (311) facets of the PbO$_{1.44}$ crystal (JCPDS card no. 27-1201). The Pb 4f XPS spectrum of the cycled PbO$_{1.44}$ NAHSs (Fig. 6j) is similar to that of the pristine PbO$_{1.44}$ NAHSs (Fig. 1l). Therein, the Pb 4f$_{5/2}$ and Pb 4f$_{7/2}$ peaks can be split into two pairs of peaks at 142.7 and 137.9 eV corresponding to Pb^{2+} and at 142.0 and 137.2 eV corresponding to Pb^{4+}, respectively. A chemical formula of PbO$_{1.563}$ can be estimated from the relative area percentages of the Pb 4f XPS peaks (i.e., Pb^{4+} (56.3%) and Pb^{2+} (43.7%)) of cycled PbO$_{1.44}$ NAHSs, which is close to the stoichiometric ratio of PbO$_{1.44}$.

In sharp contrast, severe pulverization of the cycled β-PbO$_2$ MSs electrode (Fig. 6k, S13, S14b and S15b†) was visually detected, as revealed in the upper right inset SEM image of representative cracked β-PbO$_2$ MSs. More seriously, the huge volume expansion of lithiated β-PbO$_2$ MSs caused the peeling off of active materials from the current collector (i.e., Cu foil), as indicated by the yellow arrows in Fig. 6k for the exposed areas of the current collector, resulting in the rapid degradation of the capacities of β-PbO$_2$ MSs with a short cycle life (Fig. 5a–c). As shown in the cross-sectional view SEM images of the pristine and cycled electrodes, the electrode of β-PbO$_2$ MSs (Fig. S14b and S15b†) underwent a thickness variation of 40% (i.e., from ~30 to 42 μm), which is much higher than the 14% (i.e., from ~28 to 32 μm) of the electrode of PbO$_{1.44}$ NAHSs (Fig. S14a and S15a†). To clarify the larger specific surface area of PbO$_{1.44}$ NAHSs compared to that of β-PbO$_2$ MSs, nitrogen adsorption–desorption measurements were performed. The adsorption–desorption isotherms of PbO$_{1.44}$ NAHSs and β-PbO$_2$ MSs (Fig. 6l) can be classified as type IV isotherms with a type H3 hysteresis loop. The calculated specific surface area (i.e., Brunauer–Emmett–Teller (BET) surface area) and pore volume of PbO$_{1.44}$ NAHSs (32 m^2 g^{-1} and 0.12 cm^3 g^{-1}) are significantly higher than those of β-PbO$_2$ MSs (2 m^2 g^{-1} and 0.01 cm^3 g^{-1}), respectively. More importantly, in contrast to β-PbO$_2$ MSs, the higher specific surface area of PbO$_{1.44}$ NAHSs can induce their more homogeneous mixing with the conductive agent (acetylene black) and binder (sodium alginate), thus allowing them to attach more firmly to the current collector (copper foil) (Fig. S14†). This improves the robustness of the macrostructure of the PbO$_{1.44}$ NAHSs electrode.

As illustrated comparatively in the schematic image (Fig. 6m), the drastic increase in electrode thickness, caused by the severe volume expansion of lithiated β-PbO$_2$ MSs, induces the electrode to pulverize (Fig. S15b†) and the active material to peel off from the current collector (Fig. 6k), resulting in a rapid capacity decline. In sharp contrast, the superior cycling stability and rate capability of PbO$_{1.44}$ NAHSs (Fig. 6n) can be reasonably assigned to the excellent structural features
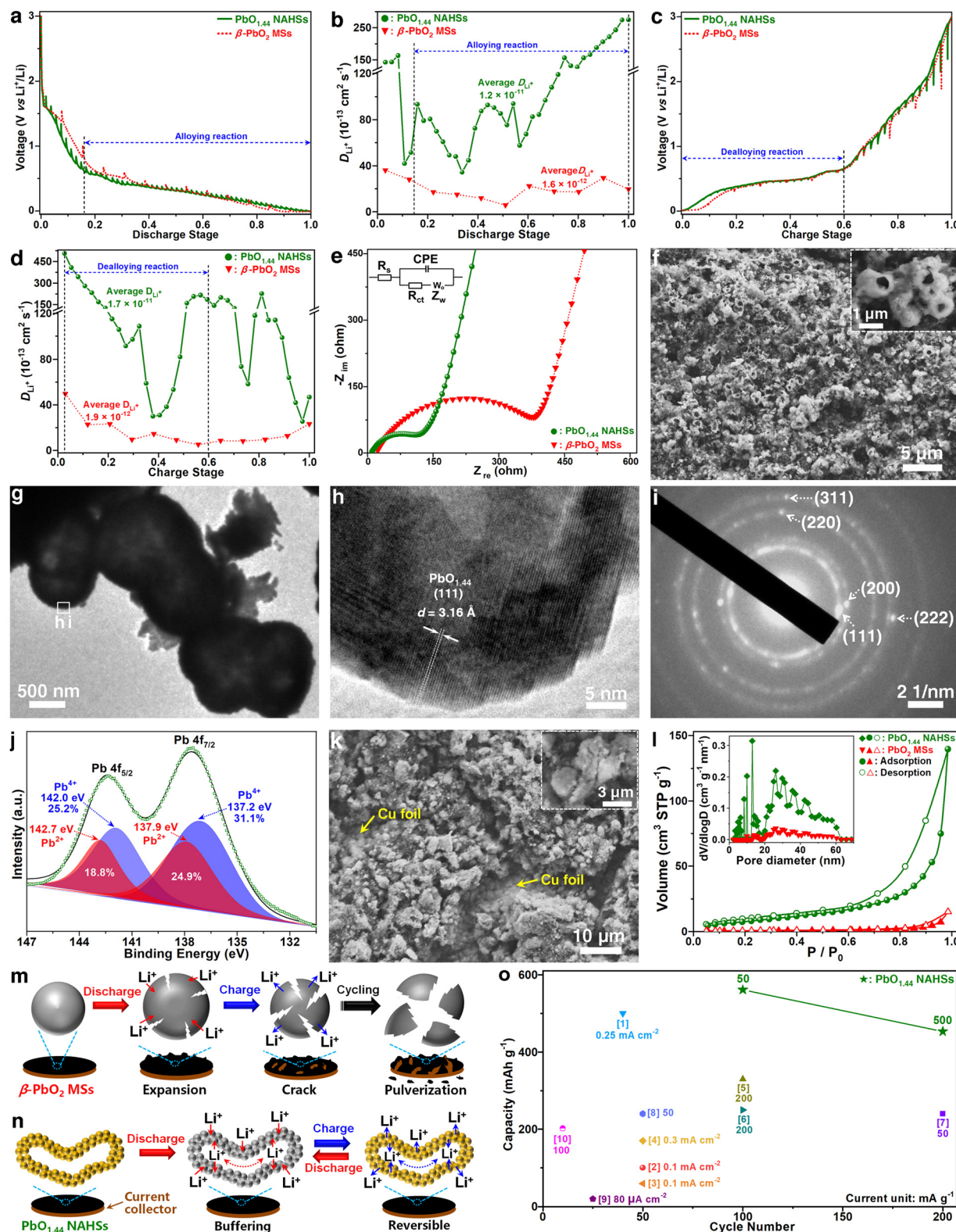
Fig. 6 Performance enhancement mechanism of PbO$_{1.44}$ NAHSs. (a and c) GITT voltage profiles and (b and d) the calculated Li$^+$ chemical diffusion coefficients based on stoichiometry from GITT of PbO$_{1.44}$ NAHSs and β-PbO$_2$ MSs during the 10th cycle at 50 mA g^{-1}. (e) Nyquist plots (inset, equivalent circuit) of cells with PbO$_{1.44}$ NAHSs and β-PbO$_2$ MSs used as anodes. (f) SEM and (g and h) TEM images, (i) SAED pattern and (j) XPS spectrum of (f–i) cycled PbO$_{1.44}$ NAHSs and (k) SEM image of cycled β-PbO$_2$ MSs after the 90th cycle in the rate performance tests. (l) Nitrogen adsorption–desorption isotherms and (inset) the pore size distributions of PbO$_{1.44}$ NAHSs and β-PbO$_2$ MSs. Schematic illustrations of (m) lithiation-induced volume expansion and pulverization of β-PbO$_2$ MSs and (n) effectively buffered volume changes combined with shortened ion transfer distance of PbO$_{1.44}$ NAHSs. (o) Performance comparison of PbO$_{1.44}$ NAHSs and reported PbO$_x$-based anodes as listed in Table S1.†

described as follows: (1) the interconnected hollow interior (Fig. 1e–g, 6f and g) with excellent volume change buffering efficiency enhances the electrode robustness for splendid cycling stability (Fig. 5a and b); (2) the short Li^+/e^- transfer distance of the secondary nanoparticles (~50 nm in diameter, Fig. 1d, h and S1a–S1f†) promotes the fast and adequate electrochemical reaction for high capacity at various C-rates (Fig. 5c); (3) the thin shells constructed from ultra-fine nanoparticles (Fig. 1d) effectively reduce the volume expansion–shrinkage of the particles caused by lithium insertion–extraction, to decrease the electrode thickness variation and improve the structural stability of the entire electrode. Owing to the excellent structural features of the nanoparticle assembly and its interconnected hollow interior, the $PbO_{1.44}$ NAHSs manifests enhanced lithium storage capability in contrast to the recently reported PbO_x-based materials (Fig. 6o and Table S1†).[10–19]

3. Conclusions

In summary, we have developed a robust strategy for the PVP-driven transformation of β-PbO_2 microspheres (MSs) to craft unique nanoparticle-assembled interconnected $PbO_{1.44}$ hollow spheres (NAHSs), which have been explored for the first time as an advanced anode material for LIBs. In particular, an intriguing PVP-driven reduction combined dissolution–recrystallization transformation process of converting β-PbO_2 MSs into $PbO_{1.44}$ NAHSs is demonstrated by PVP concentration regulation experiments. Moreover, PVP also serves as a capping agent to stabilize the $PbO_{1.44}$ solid spheres aggregated from the nanoparticles formed after 1 h of reaction and guides their inside-out Ostwald ripening to construct the interconnected hollow structure. Remarkably, $PbO_{1.44}$ NAHSs demonstrated dramatically enhanced cycling stability and rate capability in stark contrast to the performance of β-PbO_2 MSs. Based on the electrochemical analyses of the voltage plateaus and CV peaks, the superior lithium storage capability of $PbO_{1.44}$ NAHSs is primarily attributed to the effectively enhanced alloying–dealloying reaction kinetics of Pb, which is dramatically boosted by the short ion/electron transfer distance of the ultra-fine secondary $PbO_{1.44}$ nanoparticles (~50 nm in diameter). Furthermore, the ample space of the interconnected hollow interiors of $PbO_{1.44}$ NAHSs provides superb volume expansion buffering efficiency to reinforce the structural robustness of the electrode for distinguished cycling durability. As such, $PbO_{1.44}$ NAHSs with excellent lithiation–delithiation reaction kinetics and reversibility may stand out as promising low-cost and high mass/volume capacity (i.e., 561 mA h g^{-1}/5262 mA h cm^{-3}) anode candidates for LIBs. Moreover, the proposed reductant and capping dual functions of PVP and the self-sacrificial templating mechanism in the construction of the rare mixed-valence $PbO_{1.44}$ NAHSs provide new insights into the rational design of novel hollow-structured functional materials with excellent mechanical and electrochemical characteristics for various potential applications.

Author contributions

X. B. and J. Z. contributed equally to this work. All authors have given approval to the final version of the manuscript.

Data availability

All relevant data are within the manuscript and its ESI,† which are also available from the corresponding author on reasonable request.

Conflicts of interest

There are no conflicts to declare.

Acknowledgements

References

1 Y. Li, S. Song, H. Kim, K. Nomoto, H. Kim, X. Sun, S. Hori, K. Suzuki, N. Matsui, M. Hirayama, T. Mizoguchi, T. Saito, T. Kamiyama and R. Kanno, Science, 2023, 381, 50–53.

2 A. Kondori, M. Esmaeilirad, A. M. Harzandi, R. Amine, M. T. Saray, L. Yu, T. Liu, J. Wen, N. Shan, H.-H. Wang, A. T. Ngo, P. C. Redfern, C. S. Johnson, K. Amine, R. Shahbazian-Yassar, L. A. Curtiss and M. Asadi, Science, 2023, 379, 499–505.

3 S. Zhao, Z. Wang, Y. He, H. Jiang, Y. Harn, X. Liu, C. Su, H. Jin, Y. Li, S. Wang, Q. Shen and Z. Lin, Adv. Energy Mater., 2019, 9, 1901093.

4 X. Yuan, B. Liu, M. Mecklenburg and Y. Li, Nature, 2023, 620, 86–91.

5 S. Zhao, C. D. Sewell, R. Liu, S. Jia, Z. Wang, Y. He, K. Yuan, H. Jin, S. Wang, X. Liu and Z. Lin, Adv. Energy Mater., 2020, 10, 1902657.

6 X. Bo, Q. Zhang, G. Li, J. Zhang, R. Wu, S. Wang, I. K. Tiwalade, S. Wang, Z. Lin and S. Zhao, Chem. Eng. J., 2024, 487, 150559.

7 S. Zhao, Y. He, Z. Wang, X. Bo, S. Hao, Y. Yuan, H. Jin, S. Wang and Z. Lin, Adv. Energy Mater., 2022, 12, 2201015.

8 F. Xie, S. Zhao, X. Bo, G. Li, J. Fei, E.-A. M. A. Ahmed, Q. Zhang, H. Jin, S. Wang and Z. Lin, J. Mater. Chem. A, 2023, 11, 53–67.

9 J. Han, J. Park, S.-M. Bak, S.-B. Son, J. Gim, C. Villa, X. Hu, V. P. Dravid, C. C. Su, Y. Kim, C. Johnson and E. Lee, Adv. Funct. Mater., 2021, 31, 2005362.

10 M. Martos, J. Morales, R. A. L. Sánchez, D. Leinen, F. Martin and J. R. R. Barrado, *Electrochim. Acta*, 2001, **46**, 2939–2948.

11 S. H. Ng, J. Wang, K. Konstantinov, D. Wexler, J. Chen and A. H. K. Liu, *J. Electrochem. Soc.*, 2006, **153**, A787–A793.

12 K. Konstantinov, S. H. Ng, J. Z. Wang, G. X. Wang, D. Wexler and H. K. Liu, *J. Power Sources*, 2006, **159**, 241–244.

13 Q. Pan, Z. Wang, J. Liu, G. Yin and M. Gu, *Electrochem. Commun.*, 2009, **11**, 917–920.

14 H. Wang, Y. Li, Y. Wang, J. Ma, S. Hu, H. Hou and J. Yang, *Ceram. Int.*, 2017, **43**, 12442–12451.

15 C.-H. Li, P. Sengodu, D.-Y. Wang, T.-R. Kuo and C.-C. Chen, *RSC Adv.*, 2015, **5**, 50245–50252.

16 A. Guo, E. Chen, B. R. Wygant, A. Heller and C. B. Mullins, *ACS Appl. Energy Mater.*, 2019, **2**, 3017–3020.

17 Z. Chen, X. Cheng, H. Yu, H. Zhu, R. Zheng, T. Liu, J. Zhang, M. Shui and J. Shu, *Ceram. Int.*, 2018, **44**, 17094–17101.

18 F. B. F. R. Lipparoni, S. Panero and B. Scrosati, *Ionics*, 2002, **8**, 177–182.

19 L. Zhan, X. Xiang, B. Xie and B. Gao, *Powder Technol.*, 2017, **308**, 30–36.

20 P. He, Y. Yang, H. Huang, J. Huang, H. Wang, Y. He and Z. Guo, *J. Energy Chem.*, 2024, **97**, 486–497.

21 H. Wang, J. Yu, Y. Zhao and Q. Guo, *J. Power Sources*, 2013, **224**, 125–131.

22 J. P. Carr and N. A. Hampson, *Chem. Rev.*, 1972, **72**, 679–703.

23 Y. Kwon, H. Lee and J. Lee, *Nanoscale*, 2011, **3**, 4984–4988.

24 R. Inguanta, F. Vergottini, G. Ferrara, S. Piazza and C. Sunseri, *Electrochim. Acta*, 2010, **55**, 8556–8562.

25 I. Sirés, C. T. J. Low, C. Ponce-de-León and F. C. Walsh, *Electrochem. Commun.*, 2010, **12**, 70–74.

26 G. Xi, Y. Peng, L. Xu, M. Zhang, W. Yu and Y. Qian, *Inorg. Chem. Commun.*, 2004, **7**, 607–610.

27 M. Bervas, M. Perrin, S. Geniès and F. Mattera, *J. Power Sources*, 2007, **173**, 570–577.

28 M. Cao, C. Hu, G. Peng, Y. Qi and E. Wang, *J. Am. Chem. Soc.*, 2003, **125**, 4982–4983.

29 I. Petersson and E. Ahlberg, *J. Power Sources*, 2000, **91**, 137–142.

30 C. A. Sorrell, *J. Am. Ceram. Soc.*, 1973, **56**, 613–618.

31 S. Venkataraj, J. Geurts, H. Weis, O. Kappertz, W. K. Njoroge, R. Jayavel and M. Wuttig, *J. Vac. Sci. Technol., A*, 2001, **19**, 2870–2878.

32 W. Shi, S. Song and H. Zhang, *Chem. Soc. Rev.*, 2013, **42**, 5714–5743.

33 Z. Zhuang, Q. Peng and Y. Li, *Chem. Soc. Rev.*, 2011, **40**, 5492–5513.

34 Y. Xiong, J. McLellan, J. Chen, Y. Yin, Z. Li and Y. Xia, *J. Am. Chem. Soc.*, 2005, **127**, 17118–17127.

35 Y. Xiong, I. Washio, J. Chen, H. Cai, Z. Li and Y. Xia, *Langmuir*, 2006, **22**, 8563–8570.

36 Y. Xiong, J. Chen, B. Wiley, Y. Xia, Y. Yin and Z. Li, *Nano Lett.*, 2005, **5**, 1237–1242.

37 A. Ali Umar and M. Oyama, *Cryst. Growth Des.*, 2006, **6**, 818–821.

38 B. Xi, S. Xiong, H. Fan, X. Wang and Y. Qian, *Cryst. Growth Des.*, 2007, **7**, 1185–1191.

39 S. Coskun, B. Aksoy and H. E. Unalan, *Cryst. Growth Des.*, 2011, **11**, 4963–4969.

40 Y. Zhang and J. Lu, *Cryst. Growth Des.*, 2008, **8**, 2101–2107.

41 Y. Wang, J. Ren, K. Deng, L. Gui and Y. Tang, *Chem. Mater.*, 2000, **12**, 1622–1627.

42 L. Guo, Q.-J. Huang, X.-Y. Li and S. Yang, *Langmuir*, 2006, **22**, 7867–7872.

43 J. Fei, S. Zhao, X. Bo, F. Xie, G. Li, E.-A. M. A. Ahmed, Q. Zhang, H. Jin and Z. Lin, *Carbon Energy*, 2023, **5**, e333.

44 S. Zhao, Z. Wang, Y. He, B. Jiang, Y. Harn, X. Liu, F. Yu, F. Feng, Q. Shen and Z. Lin, *ACS Energy Lett.*, 2017, **2**, 111–116.

45 B. Jiang, Y. He, B. Li, S. Zhao, S. Wang, Y.-B. He and Z. Lin, *Angew. Chem., Int. Ed.*, 2017, **56**, 1869–1872.

46 S. Zhao, Y. Wang, R. Liu, Y. Yu, S. Wei, F. Yu and Q. Shen, *J. Mater. Chem. A*, 2015, **3**, 17181–17189.

47 M. Y. Yang, S. V. Zybin, T. Das, B. V. Merinov, W. A. Goddard, E. K. Mok, H. J. Hah, H. E. Han, Y. C. Choi and S. H. Kim, *Adv. Energy Mater.*, 2022, **13**, 2202949.

48 W. Weppner and R. A. Huggins, *J. Electrochem. Soc.*, 1997, **124**, 1569.

49 X. Xu, F. Xu, C. Qu, G. Jiang, H. Yu, H. Repich, H. Han, F. Cao, L. Li and H. Wang, *Adv. Funct. Mater.*, 2021, **31**, 2101059.